GFZ
Helmholtz-Zentrum
POTSDAM

Originally published as:

Bufe, A., Turowski, J., Burbank, D. W., Paola, C., Wickert, A. D., Tofelde, S. (2019): Controls on the lateral channel-migration rate of braided channel systems in coarse non-cohesive sediment. - *Earth Surface Processes and Landforms*, *44*, 14, pp. 2823—2836.

DOI: http://doi.org/10.1002/esp.4710

EARTH SURFACE PROCESSES AND LANDFORMS
Earth Surf. Process. Landforms **44**, 2823–2836 (2019)
© 2019 The Author. Earth Surface Processes and Landforms published by John Wiley & Sons, Ltd.
Published online 14 August 2019 in Wiley Online Library
(wileyonlinelibrary.com) DOI: 10.1002/esp.4710

Controls on the lateral channel-migration rate of braided channel systems in coarse non-cohesive sediment

Aaron Bufe,[1]* Jens M. Turowski,[1] Douglas W. Burbank,[2] Chris Paola,[3] Andrew D. Wickert[3] and Stefanie Tofelde[4]
[1] GFZ German Research Center for Geosciences, Potsdam, Germany
[2] Department of Earth Sciences, University of California, Santa Barbara, CA, USA
[3] Department of Earth Sciences and Saint Anthony Falls Laboratory, University of Minnesota, Twin Cities, Minneapolis, MN, USA
[4] Institute for Environmental Sciences and Geography, University of Potsdam, Potsdam, Germany

Received 1 March 2019; Revised 30 June 2019; Accepted 23 July 2019

*Correspondence to: Aaron Bufe, GFZ German Research Center for Geosciences, Telegrafenberg, 14473 Potsdam, Germany. E-mail: abufe@gfz-potsdam.de
This is an open access article under the terms of the Creative Commons Attribution License, which permits use, distribution and reproduction in any medium, provided the original work is properly cited.

ESPL
Earth Surface Processes and Landforms

ABSTRACT: Lateral movements of alluvial river channels control the extent and reworking rates of alluvial fans, floodplains, deltas, and alluvial sections of bedrock rivers. These lateral movements can occur by gradual channel migration or by sudden changes in channel position (avulsions). Whereas models exist for rates of river avulsion, we lack a detailed understanding of the rates of lateral channel migration on the scale of a channel belt. In a two-step process, we develop here an expression for the lateral migration rate of braided channel systems in coarse, non-cohesive sediment. On the basis of photographic and topographic data from laboratory experiments of braided channels performed under constant external boundary conditions, we first explore the impact of autogenic variations of the channel-system geometry (i.e. channel-bank heights, water depths, channel-system width, and channel slope) on channel-migration rates. In agreement with theoretical expectations, we find that, under such constant boundary conditions, the laterally reworked volume of sediment is constant and lateral channel-migration rates scale inversely with the channel-bank height. Furthermore, when channel-bank heights are accounted for, lateral migration rates are independent of the remaining channel geometry parameters. These constraints allow us, in a second step, to derive two alternative expressions for lateral channel-migration rates under different boundary conditions using dimensional analysis. Fits of a compilation of laboratory experiments to these expressions suggest that, for a given channel bank-height, migration rates are strongly sensitive to water discharges and more weakly sensitive to sediment discharges. In addition, external perturbations, such as changes in sediment and water discharges or base level fall, can indirectly affect lateral channel-migration rates by modulating channel-bank heights. © 2019 The Author. Earth Surface Processes and Landforms published by John Wiley & Sons, Ltd.

KEYWORDS: braided alluvial rivers; physical experiments; channel migration

Introduction

The lateral movement of channels across fluvial surfaces is a fundamental characteristic of alluvial river systems. The rate of this lateral movement controls the dynamics and scales of diverse landscapes, such as deltas, floodplains, alluvial fans, and alluvial sections of bedrock rivers (Figure 1). Lateral river movement influences, for example, the construction of stratigraphy (Paola et al., 2001; Martin et al., 2009; Straub et al., 2013), the planation of uplifting topography (Hancock & Anderson, 2002; Bufe et al., 2016), and the storage time of sediment on floodplains (Nakamura & Kikuchi, 1996; Bradley & Tucker, 2013; Torres et al., 2017) or in fluvial terraces (Limaye & Lamb, 2016; Malatesta et al., 2017). Moreover, plant and animal habitats (Scott et al., 1997; Shields et al., 2002), land-use potential, and flooding hazards (Hutton & Haque, 2004) can be directly affected by lateral river movement. Channels move laterally through two main mechanisms: abrupt rerouting of water into new channels by avulsions (Slingerland & Smith, 2004) and gradual sideways migration of individual channels (Einstein, 1926; Hickin & Nanson, 1984). Here, we focus on the gradual lateral migration (as opposed to avulsions) of braided alluvial river systems.

We currently lack a model for the reworking rate of an alluvial surface where gradual migration of braided channels dominates lateral channel movements. Detailed models exist for the erosion rate of a single channel bank with known geometry as a function of the shear-stress distribution along the channel bank and the resistance of banks to erosion (Hanson & Simon, 2001; Darby et al., 2007; Darby et al., 2010). Moreover, hydrodynamic relations exist for the migration of river meanders as a function of the channel curvature (Einstein, 1926; Howard & Knutson, 1984; Parker et al., 2011), and these relations have been successfully incorporated into numerical models

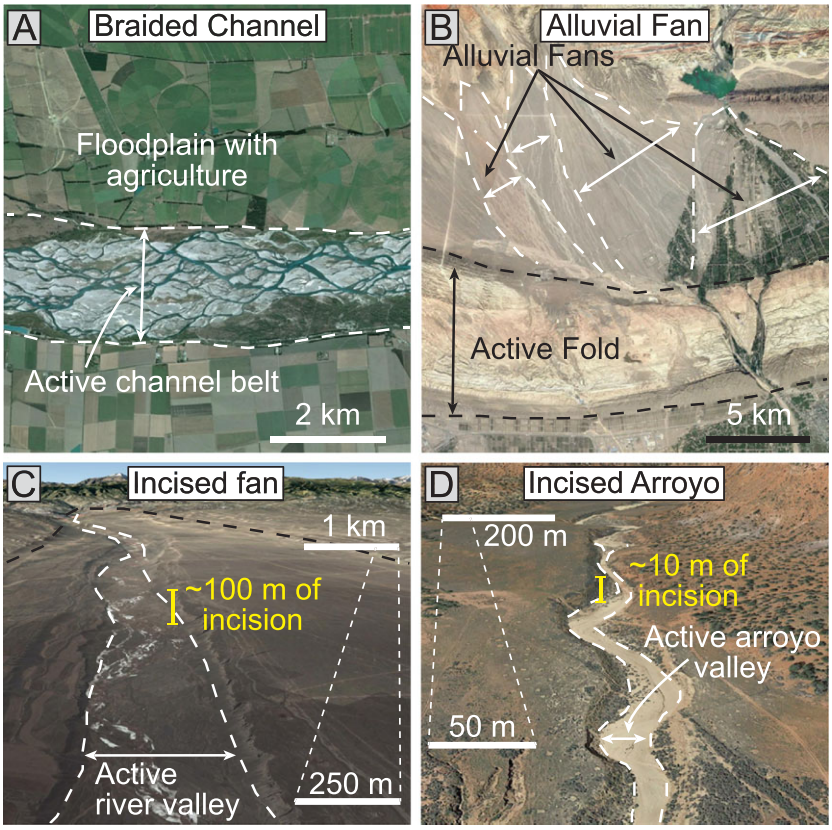

Figure 1. Examples of areas that are actively reworked by laterally moving channels (bounded by white dashed lines). GoogleEarth® images of (A) active braidplain of the Rakaia River near Barrhill, New Zealand (latitude S43.67, longitude E171.88); (B) central Atushi fold and Boguzihe river alluvial fans, north of Kashgar, Xinjiang, China (latitude ~N39.76, longitude ~E75.99); (C) incised alluvial fan west of Urumqi, Xinjiang, China (latitude ~N43.99, longitude ~E86.77); and (D) incised Kitchen Corral Wash in the Vermillion Cliffs, Utah, USA (latitude ~N37.21, longitude ~W112.13). [Colour figure can be viewed at wileyonlinelibrary.com]

(Howard & Knutson, 1984; Coulthard & Wiel, 2006; Limaye & Lamb, 2014; Langston & Tucker, 2018). However, it remains challenging both (1) to upscale models of migration of single meanders or channel banks to the rate of reworking of an entire channel belt (Wickert et al., 2013) and (2) to understand the sensitivity of migration to internal (autogenic) dynamics and external (allogenic) forcing (Muto et al., 2007; Martin et al., 2009; Wickert et al., 2013; Constantine et al., 2014). Here, we focus on lateral migration on the scale of a channel system as opposed to the scale of individual channels or channel banks. We use data from published laboratory experiments and dimensional analysis to develop two alternative expressions for the lateral migration rate of braided channel systems in non-cohesive sediments. These expressions link the lateral migration rate to the channel-bank height and, respectively, (1) the input sediment and water discharges and (2) the water depth, channel slope and channel-system width. Finally, we discuss the sensitivity of migration rates to different boundary conditions both in steady state and in perturbed systems.

Lateral channel-migration rates of braided alluvial channels

Most alluvial channels migrate back and forth across an active fluvial surface that is relatively stable through time. Here we consider two parameters that describe the spatial and temporal pattern of fluvial-surface reworking on a timescale that is linked to the migration rate: the average (instantaneous) lateral migration rate (M_L) of a system of channels and the area that is actively reworked by such channel systems (A_{act}). In addition, we use the term 'channel-system geometry' to include the average channel slope (S), the average water depth (H_W), the channel-system width (W_{cs}), defined as the sum of the width of all adjacent channels, and the 'effective channel-bank height' or just 'channel-bank height' (H_b) (Figure 2). The effective channel-bank height is a characteristic length scale for the height of the sediment walls that are laterally eroded. We define it here as the average height difference between the thalweg of every active channel and the mean elevation within the area that is actively reworked by each channel. This effective channel-bank height includes both the relief within the floodplain and the height of the valley walls that are actively reworked (see discussion of these two heights in Malatesta et al., 2017). Finally, we use the term 'external boundary conditions' to include the input water discharge (Q_w), sediment discharge (Q_s), sediment grain size (D), subsidence rate (or uplift rate) of the active area ($\dot{Z}_{SR}$, with positive values for subsidence and negative values for uplift), and base-level rise (or fall) rate ($\dot{Z}_{BL}$, with positive values for base-level rise and negative values for base-level fall) (see table of notations at the end of the article). We distinguish between subsidence (or uplift) rates and base-level changes, because they affect the geometry of the basin differently except where subsidence is uniform across the entire basin.

Early investigations suggest that lateral channel-migration rates depend most strongly on the channel-bank height, the water discharge, and the resistance of channel banks to erosion (Hickin & Nanson, 1984; Nanson & Hickin, 1986). In addition, a possible influence of the input sediment discharge on channel-migration rates was suggested in the 1980s (Nanson

© 2019 The Author. Earth Surface Processes and Landforms published by John Wiley & Sons, Ltd.

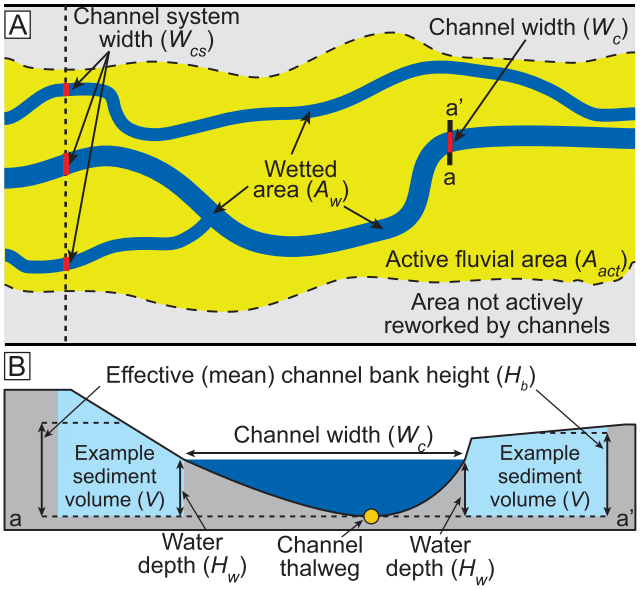

Figure 2. Conceptual plan-view sketch (A) and cross-section a–a′ (B) of an active alluvial surface with laterally migrating channels. The channel-system width (W_{cs}) is the sum of all channel widths (W_c) along a cross-section. Blue shaded areas depict an example for the same volume of sediment on both channel margins. Note that lower average bank heights imply wider sediment packages (as on the right side) that can be reworked by a channel with the capacity to rework some given volume (V) of sediment. [Colour figure can be viewed at wileyonlinelibrary.com]

& Hickin, 1983; Howard & Knutson, 1984), but has been difficult to disentangle from variations in water discharge (Hickin & Nanson, 1984). More recently, the sediment discharge has been proposed as a major control on lateral migration rates, both in meandering channels in the field and in braided experimental channels (Dunne et al., 2010; Wickert et al., 2013; Constantine et al., 2014; Bufe et al., 2016). This control was hypothesized to emerge because sediment discharge drives the rate of bar formation that in turn affects the cross-channel acceleration of flow and lateral migration rates (Dunne et al., 2010; Wickert et al., 2013).

A key challenge for finding a general expression that describes lateral channel-migration rates in braided channels is the covariation of the channel-system geometry and the external boundary conditions. For example, a change in the external input of sediment discharge within a river system could affect channel-migration rates directly by modulating the rate of bar formation (Dunne et al., 2010; Wickert et al., 2013), or indirectly by modulating the channel-system geometry (Gilbert, 1877; Mackin, 1948; Lane, 1955). Variations of channel-system geometry in response to changes in boundary conditions may be temporary and depend on the existing state of the system (Tofelde et al., 2019; Wickert & Schildgen, 2019). Therefore, in order to avoid apparent co-variations between boundary conditions and lateral channel-migration rates, it is useful to separate the effect of channel-system geometry from the direct effects of different boundary conditions on channel-migration rates.

In order to isolate the role of channel-system geometry and boundary conditions on lateral channel-migration rates, here we first study a suite of physical experiments of braided channels in non-cohesive sediments in which the channels are subject to the same constant boundary conditions (base level, water discharge, sediment discharge, and sediment grain sizes). Under such constant boundary conditions, all channel-geometry variations are due to internal (autogenic) reorganizations of water and sediment discharges (Kim et al., 2014). Therefore, these experiments allow us to isolate the controls of channel-system geometry on lateral channel mobility independently of the external boundary conditions. The constraints obtained from this investigation are then used to derive expressions for the lateral migration rate of an alluvial channel system under different boundary conditions. We test these expressions against a compilation of laboratory experiments that constrain lateral channel-migration rates in systems with variable water discharges, sediment discharges, sediment grain sizes, subsidence rates, and rates of base level rise.

Methods

In this section, we first describe a series of previously published experiments that we re-analyzed to study autogenic effects on lateral channel-migration rates. We then describe a compilation of published data that we combined with our new results to investigate lateral migration rates under varying boundary conditions.

Experimental setup

Photographic and topographic data from four previously published laboratory experiments performed in 2014 at the St Anthony Falls Laboratory (Bufe et al., 2016) are used to study variations of lateral channel-migration rates under constant boundary conditions. In each experiment, a rectangular box with dimensions of 4.8 m × 3.0 m × 0.6 m was filled with well-sorted quartz sand ($D_{50} \approx 0.52$ mm) (Figure 3). A steady flow of blue-dyed water and the same quartz sand were fed from a point source using a constant-head tank and a sediment feeder. Sediment and water were mixed and fed into the basin through a pebble-filled wire mesh to generate a diffuse influx of water and sediment (Figure 3). The base level was held constant by a weir at the downstream end of the basin across which excess water and sediment flowed into a drain (Figure 3). At the start of each experiment, the slope of the sediment fill was manually set to be slightly lower than the transport slope, and the initial sediment surface was smoothed with a shovel and broom. Thus, the channels started by aggrading and eventually came to a 'bypass' state during which the system oscillated between basin-wide aggradation and incision, but the rate of volumetric surface change remained below ~20% of the sediment influx (Bufe et al., 2016). These experiments allowed us to investigate channel movements under constant boundary conditions both during autogenic aggradational and incisional phases. Because the initial slope was manually set based on observations of channel movements in the basin, it varied between experiments, and the time to reach the bypass state ranged from ~2 to 10 hours. The original experimental series comprised six runs (Runs 1–6) that include the uplift of a fold in the center of the basin (Bufe et al., 2016). From each of Runs 1, 2, and 5 we used 5–25 hours of useable data that were collected before the uplift started. In addition, we use Run 7, which was performed for 57 hours without uplift (Supporting Information Table S1). Runs 3, 4, and 6 had fewer than five hours of useable data without uplift and are not considered in this work. All experiments used here were subject to the same water discharge ($Q_w = 790 \pm 10$ mL/s), but the input sediment discharge was set to $Q_s = 15.8 \pm 0.2$ mL/s in Runs 1, 2, and 7, and to $Q_s = 2.4 \pm 0.2$ mL/s in Run 5. Both water and sediment discharges were calibrated volumetrically using a 1-l graduated cylinder and a stopwatch to measure the rate of volume delivered by the constant head tank and the sediment feeder. Except for the lower sediment discharge of Run 5 and

© 2019 The Author. Earth Surface Processes and Landforms published by John Wiley & Sons, Ltd.

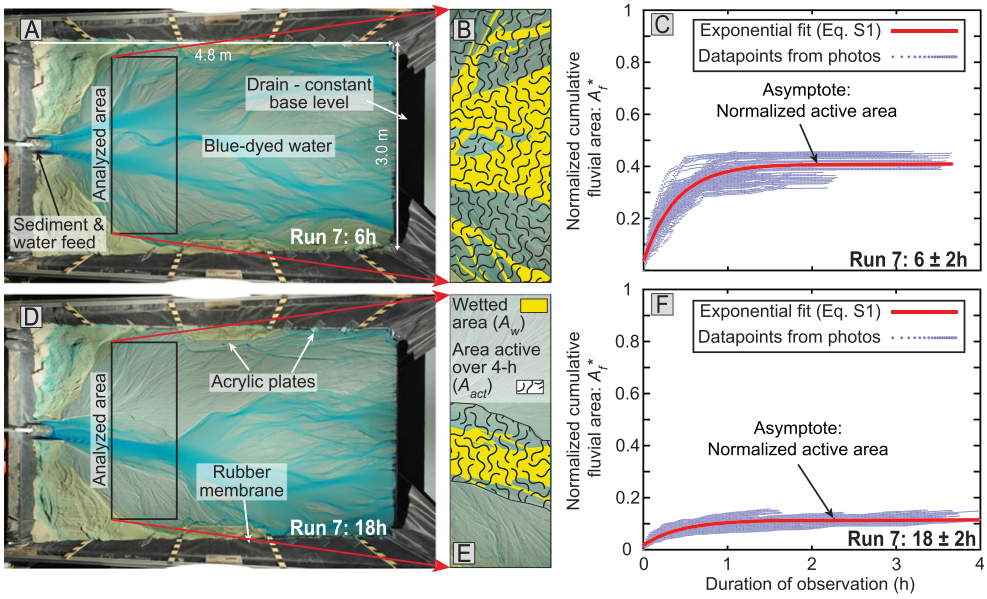

Figure 3. Experimental setup and channel-mobility calculations. (A) Overhead photograph of Run 7 at six hours. Only the black rectangle was analyzed. (B) Analyzed area of Run 7 at six hours with the wetted area and active area marked by polygons with yellow color and wavy lines, respectively. (C) Normalized cumulative fluvial area (see Supporting Information Text S2) over time for the time interval six hours ± two hours. Blue dots: data points; red line: exponential fit. The asymptote of the exponential fit is the normalized active area (A^*_{act}) (see Text S2). (D, E) Same as A and B for Run 7, but at 18 hours. (F) Same as C for Run 7 at 18 hours ± two hours. [Colour figure can be viewed at wileyonlinelibrary.com]

variations in the manually-set slopes of the initial basin fill, all experiments had identical boundary conditions.

Data collection and analysis

In order to track channel movements, we identified the blue-dyed water in overhead photographs collected at one-minute intervals at a resolution of 1 mm, and we generated binary images with a value of zero for dry pixels and a value of one for wet pixels. The channel-system geometry was measured on topographic scans with a horizontal and vertical resolution of ~1 mm that were collected every hour using a custom-built laser scanner (see Supporting Information Text S1 for more detail).

The channel-system geometry and lateral migration rates could significantly vary downstream (Figures 3A and 3D). In order to obtain representative average measurements of channel geometry for a given time, we therefore restricted the analysis to a rectangle that spanned 0.90 m (down basin) × 2.66 m (across basin). This rectangle was located 0.70 m downstream of the sediment and water feed (Figures 3A and 3D) in order to (1) minimize the effect of downstream reorganization of water and sediment discharges and (2) maximize the autogenic variability of channel-system geometry in time (Figures 3A and 3D).

The discrepancy in temporal scales between the photographic data (used to track mobile channels) and topographic data (used to measure channel-system geometry) posed a challenge. Information on channel positions was collected every minute, but topographic information was limited to hourly intervals. The active area, which defined the length-scale over which the effective channel-bank height was measured, had to be calculated over timescales long enough to allow the system to rework the entire active area (typically > one to two hours, see Figures 3C and 3F, Supporting Information Figures S2–S7). Here we chose to measure the actively reworked area using the photographic data in four-hour intervals with a one-hour spacing (For example 0–4 hours, 1–5 hours, 2–6 hours, etc.), and we averaged lateral migration rates across these four-hour time intervals. In turn, we measured channel-system geometry from topographic data collected at the midpoint of each four-hour interval.

Instantaneous lateral channel mobility (M_L)

A spatially averaged instantaneous channel mobility (M_L) was calculated for each of the four-hour time intervals. Starting with the second image in a block, the binary pixels (wet versus dry) in each image were compared to those in the previous binary, and the number of pixels that changed from dry to wet were counted. Where gaps in the photographic data exceeded two minutes, those image pairs were discarded. The number of dry-to-wet pixels, which represents channel motion, was then divided by the time interval between the two images (typically one minute) and the length of the channel system. Here we took the downstream length of the analyzed rectangle (L_b = 0.9 m) as a representative length scale of the channel system. For all channel-mobility values across each four-hour interval, the mean and its standard error were calculated. This calculation yielded an average rate of lateral fluvial surface reworking per downstream length of the analyzed system, and interpreting this reworking rate as a lateral channel-migration rate assumes that most wetted areas are channelized. Especially during phases of aggradation, some of the measured surface reworking may occur by unchannelized sheet flow, which we did not constrain here. We also emphasize that the migration rates apply to the entire channel system and are agnostic to the number and dynamics of single channels.

Fluvial-surfaces reworking and channel-system width (A_{act}, A_w, W_{cs})

As channels move across a surface, over time, the area that they have visited increases, and this increase can be approximated as an exponential approach to an asymptote (Martin et al., 2009; Bradley & Tucker, 2013;Wickert et al., 2013 ; Bufe et al., 2016). Here, we defined this asymptotic value as the 'active fluvial surface' (A_{act}) (Figures 2 and 3). We followed previous work to calculate the actively reworked fluvial surface from experimental data (Wickert et al., 2013; Bufe et al., 2016)

© 2019 The Author. Earth Surface Processes and Landforms published by John Wiley & Sons, Ltd.

within each four-hour interval (see Text S2 for details). In addition to the actively reworked area, we also calculate the average wetted area (A_w) from all images within the time interval (Table S1). Finally, the average channel-system width (W_{cs}) was calculated as the width of the analyzed box (W_b) scaled by the fraction of the wetted area within the total analyzed area (A_{tot}): $W_{cs} = \frac{A_w}{A_{tot}} W_b$.

Aggradation rates ($\dot{H}$) and channel geometry (W_c, H_w, S and H_b) Across each four-hour interval, average volumetric aggradation rates ($\dot{H}$) were measured by differencing the two topographic scans at the start and at the end of the interval, summing the difference values for all pixels, and dividing by the time interval, i.e. four hours (Table S1). The result is a volumetric rate of aggradation (positive $\dot{H}$) or erosion (negative $\dot{H}$). In addition, we calculated channel-system geometry parameters using the scan at the center of each four-hour interval. The channel positions in each scan were estimated by overlaying the topographic scan and the binary 'wet versus dry' decomposition of the last photograph taken a maximum of one minute before the scan (Figure 4). Then, for each row of 1-mm pixels, we extracted the topography along cross-sections perpendicular to the down-basin direction (Figure 4). On every cross-section, we considered each uninterrupted wet line segment as a channel with two margins that are defined by the endpoints of the line (Figure 4). This procedure of mapping channels presents two major limits. First, most channels flow obliquely to the cross-section and, second, channels move within the 30 ± 30 seconds that pass between the collection of the photograph and the topographic scan. Whereas these limits introduce biases in our measurements, they appear to be negligible on the scale of the topographic changes that we observe (see Text S3 for a full discussion).

We estimated average values of the channel slope (S) by a linear regression through the highest thalweg in each cross-section, and channel width (W_c) as the horizontal distance between channel margins. In addition, we measured the flow depth (H_w) for every channel as the height between the thalweg (the lowest elevation within each channel cross-section) and the lowest elevation channel margin. The effective channel-bank heights (H_b) for both channel margins were measured as the sum of the flow depth (H_w) and the elevation difference between the channel margin and the peak elevation of the sediment surface within a given search distance (d_s) (Figure 4B). For each channel, right and left bank heights were then averaged to yield an average effective channel-bank height. Above, the effective bank height was defined as the mean elevation of the banks above the thalweg. Here, we extracted the peak elevation of the sediment surface within the search distance, because of the biases introduced by projecting a radial alluvial fan on parallel lines (Figure 4, see Text S3 for a detailed discussion). The distance from the channel center over which the peak elevation of the sediment surface was searched (d_s) was set to the channel half-width scaled by the active fluvial area. The assumption behind this search distance is that each channel is responsible for reworking a fraction of the total active area that is set by the fraction of the wetted area that it occupies. We note that using a constant fraction of the channel half-width (between one and two times $\frac{1}{2} W_c$) as the search distance does not affect the bank height significantly (see Text S3 for more detail). As a last step, we calculated the mean and standard error for channel widths, flow depths, and channel-bank heights (W_c, H_w, and H_b) of all streams in all cross-

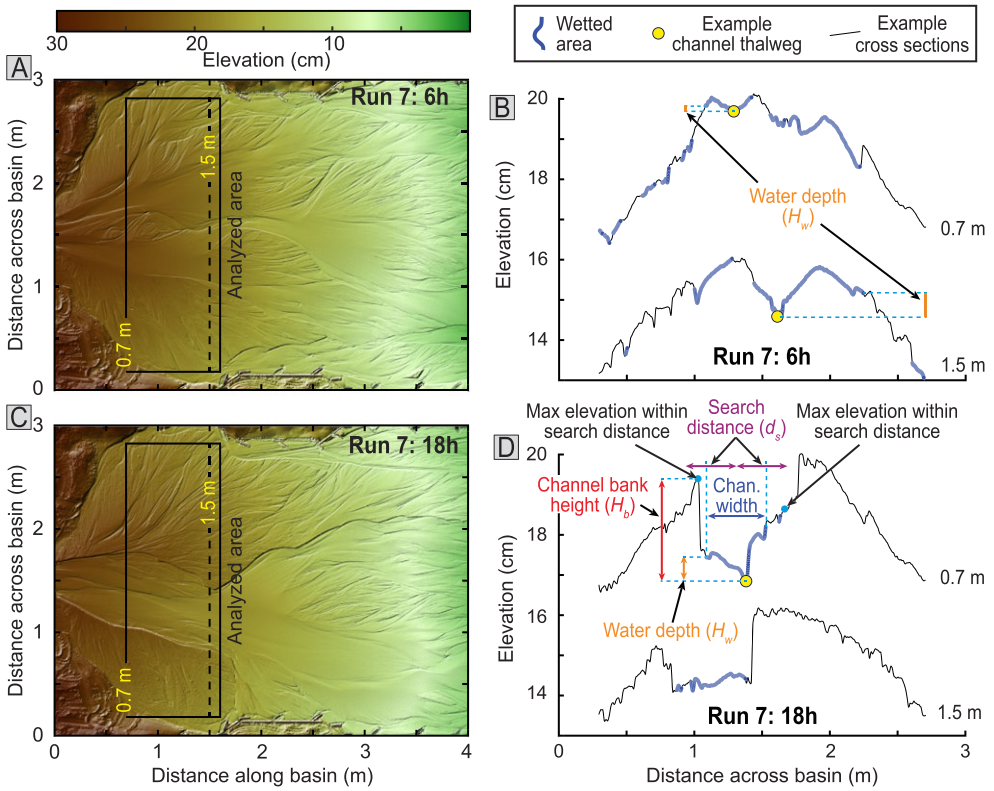

Figure 4. Topographic scans and cross-sections for Run 7. (A, C) Topographic scans of Run 7 at six and 18 hours, respectively. Black rectangles mark the analyzed area. Topographic analysis was performed along 1-mm-spaced cross-sections. Example cross-sections are shown at 0.7 m and 1.5 m from the water/sediment input. (B, D) Cross-sections from A and C shown in black. Blue lines denote wetted sections from photographs taken < 120 seconds before the scan. Each uninterrupted wet section > 10 mm in width is considered a channel. Yellow dots mark the highest channel thalweg in each cross-section. Bank heights on both sides of the channel were averaged to yield a bank height for each channel (see Methods section). [Colour figure can be viewed at wileyonlinelibrary.com]

© 2019 The Author. Earth Surface Processes and Landforms published by John Wiley & Sons, Ltd.

sections to obtain a single average measure of these topographic metrics for every scan at the center of the four-hour interval (Table S2). For the flow depth (H_w) and the effective channel-bank height (H_b), this mean was weighted by the channel width (W_c) such that larger channels contribute more strongly to the average value (see Text S3 for more detail on the measurement of the channel-system geometry).

Relative importance of avulsions and lateral migration

In order to determine the dominant process of lateral channel movement, we estimated the relative timescales of avulsions and lateral migration (T^*_{A-M}) following Jerolmack and Mohrig (2007) as:

$$T^*_{A-M} = \frac{T_A}{T_M} = \frac{M_L}{W_{cs}} \times \frac{A_w H_w}{\dot{H}}, \quad (1)$$

where $\dot{H}$ is the average aggradation rate within the analyzed area, $T_A = \frac{A_w H_w}{\dot{H}}$ is a characteristic timescale of avulsion, i.e. the time to aggrade one channel depth worth of sediment, and $T_M = \frac{W_{cs}}{M_L}$ is a characteristic timescale of lateral migration, i.e. the timescale to migrate one channel width. For values of $T^*_{A-M} > 1$, channel migration dominates lateral channel movements, whereas for $T^*_{A-M} < 1$, channel avulsions dominate (Jerolmack & Mohrig, 2007).

Compilation of experiments

In order to test the sensitivity of lateral migration rates under different boundary conditions, we draw on a previous compilation of physical experiments that are all characterized by a steady input of sediment and water across a bed of non-cohesive sediment (Wickert et al., 2013). The compilation includes (1) two alluvial fan-delta experiments (DB03-01 and DB03-02) that were steadily aggrading at equilibrium with the rate of sea-level rise (Martin, 2007; Sheets et al., 2007), (2) one alluvial fan delta subject to a basin-subsidence rate of ~1.85 mm/h and separately analyzed phases of steady base level (XES02-SS), rising base level (XES02-SR and XES02-RR), and falling base level (XES02-SR and XES02-RR) (Kim et al., 2006, 2006), and (3) one braided channel experiment (BV-1) that was performed at steady base level (Table S2) (Tal & Paola, 2007, 2010). We did not include the last experiment in the original compilation (BV-2 in Wickert et al., 2013). Because BV-2 is the only experiment in the compilation that has sediment banks with cohesion, we have insufficient data for a systematic investigation of the controls of bank cohesion on lateral migration rates. We also note that DB03-02 is characterized by a very low sediment discharge and subcritical flow, unlike all the other experiments, which exhibit dominantly supercritical flow. Similar to our analysis, lateral migration rates in all experiments were calculated by Wickert et al. (2013) by comparing the change in the channel position (the wetted area) between adjacent images and averaging the movement across the entire length of the basins. In contrast to our experiments, these lateral migration rates were calculated across the entire fluvial surface and not just in a limited upstream part of the basin. Therefore, they may be more strongly affected by autogenic reorganizations of sediment and water discharges across the basin. In addition, avulsions are common in the three aggrading delta experiments and cause anomalously high reworking rates in those image pairs that capture avulsion events. Such events could lead to some overestimate of the average rate of lateral channel migration. The channel-bank heights in these experiments were quantified by measuring average bankfull channel depth manually or with a laser on the dried experimental surfaces (Kim, Paola, Swenson, & Voller, 2006; Kim, Paola, Voller, & Swenson, 2006; Martin, 2007; Sheets et al., 2007; Tal & Paola, 2007, 2010; Wickert et al., 2013). Because all experiments had negligible incision, this bankfull channel depth is expected to be within uncertainty of the effective channel-bank height that was calculated in our analysis. In order to compare a single data point from each of our experiments to this compilation, we averaged the values from all four-hour intervals across each of Runs 1, 2, 5, and 7 (Table S2).

Results from Experiments of this Study

In all runs, a network of highly mobile braided channels reworked the fluvial surface. Prior to the start of our measurements, the basin rapidly aggraded (Figure 5A), because the initial slope of the basin was set to just below the transport slope for the input sediment and water discharges. Within the first ~5–10 hours, aggradation rates decreased, and the system alternated between overall deposition and erosion (Figure 5A). Runs 1 and 2 (high Q_s) yielded eight and two usable four-hour time-intervals over 13 and 5 hours of run time, respectively (Table S1). These runs always remained in the initial aggradation phase (Figure 5A) and were characterized by a relatively wide channel system (Figure 5B) with low effective bank heights (Figure 5C) and a high lateral migration rate (Figure 5D). In Run 7 (high Q_s), we used 32 time-intervals within 57 hours of run time. At the beginning of this experiment, the rates at which sediment volumes aggraded in the analyzed area were ~6% of the input sediment discharge and decreased over eight hours (Figure 5A). Importantly, despite similar boundary conditions to Runs 1 and 2, after approximately eight hours of run time, a phase of autogenic incision occurred, and most water became concentrated into one incised channel (Figure 3D). This incision led to a relatively low channel-system width, high bank heights, and low lateral migration rates (Figures 5B–5D). Over the course of Run 7, channels widened and the depth of incision decreased (Figures 5B and 5C), but, in the analyzed area, the channels' active surface never reached their initial extent. Given the similarity in the boundary conditions of Runs 1, 2, and 7, we hypothesize that Runs 1 and 2 would have eventually also experienced such a phase of autogenic incision, but they were not run for a long-enough time period.

In addition to these high sediment-discharge experiments, we also analyzed 19 four-hour time intervals spanning 25 hours of time of Run 5. Run 5 was performed at an approximate seven-fold lower input sediment discharge than the other experiments. This experiment included time intervals of overall deposition and overall erosion (Figure 5A), and the lateral migration rates, channel-bank heights, and channel-system widths fell within the range of the high Q_s experiments (Figures 5B–5D). Throughout all experimental series, we found mobility numbers (T^*_{A-M}) of > 1 (and frequently > 4) (Jerolmack & Mohrig, 2007), even during the most rapidly aggrading time periods (Table S1). These mobility numbers imply that lateral migration tended to dominate over avulsion. Nevertheless, for the most rapidly aggrading periods where channel mobility numbers are close to one, some overestimate of lateral migration rates may have occurred due to avulsions.

© 2019 The Author. Earth Surface Processes and Landforms published by John Wiley & Sons, Ltd.

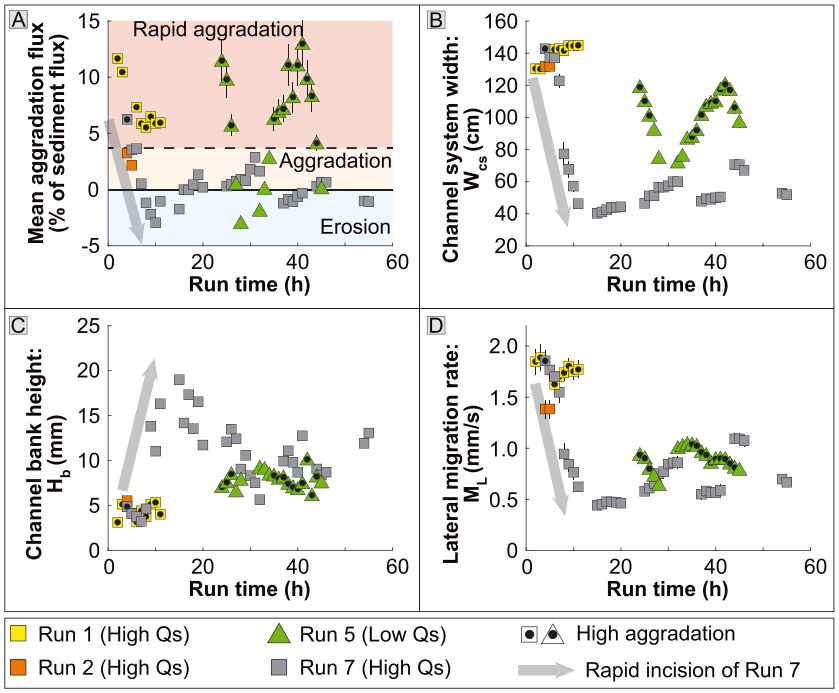

Figure 5. Time series of data averaged across four-hour intervals as a function of the run time at the midpoint of the four-hour interval. (A) Average aggradation rates relative to sediment discharge. Shading shows regions of erosion, aggradation, and 'rapid aggradation'. The latter denotes aggradation rates that are above the long-term range of aggradation rates in Run 7. (B) Channel-system width. (C) Effective channel-bank height. (D) Lateral migration rate. [Colour figure can be viewed at wileyonlinelibrary.com]

Discussion

Controls on lateral migration rates under constant boundary conditions

The data from Runs 1, 2, and 7 (high Q_s) allow us to investigate a channel system under constant boundary conditions. Here, all changes in channel-system geometry are caused by internal (autogenic) dynamics, and we can isolate the impact of channel-system geometry on lateral migration rates independently of the boundary conditions. Based on existing models for the controls of channel-bank heights on lateral channel-migration rates (Nanson & Hickin, 1986; Malatesta et al., 2017), we hypothesize that a channel system that is adjusted to constant boundary conditions has the capacity to rework a constant volume of sediment within a given time. The volumetric rate of sediment reworking (M_V) is the lateral migration rate (M_L) multiplied by a characteristic channel-system length (L_c) and the height of the reworked sediment banks (taken here as the effective channel-bank height H_b):

$$M_V = L_c H_b M_L = \text{constant with constant boundary conditions} \quad (2)$$

If this hypothesis is correct, and assuming a constant length of the channel system, the impact of autogenic changes in the channel-system geometry on lateral erosion rates will yield an inverse scaling of lateral migration rates with the channel-bank height:

$$M_L = \frac{M_V}{L_c H_b}. \quad (3)$$

Indeed, we find that average lateral migration rates (M_L) scale with the effective channel-bank height, (H_b) ($r^2 = 0.81$) (Figure 6A). Using the water depth, H_w, instead of the effective channel-bank height, produces a poorer fit ($r^2 = 0.63$) (Figure S1A). The scatter in the relationship between migration rates and bank height could stem from random fluctuations in the channel-system length (L_c) that are not accounted for (see Equation (3)), from measurement limitations, or from the influence of some other parameter that we did not consider. The best-fit exponent of the power law (-0.84 ± 0.06 ($\pm 1\sigma$)) is quite close to the expected value of –1 (Figure 6A), and an inverse fit of migration rates to channel-bank heights, i.e. with power-law exponent of –1, describes the data well ($r^2 = 0.78$) (Figure 6A). This finding suggests that for constant boundary conditions, the volume of reworked sediment is close to constant and that our proposed model (Equations (2) and (3)) can explain most of the variability in the migration rates. If our model is correct, the small difference of the best fit from the expected power-law exponent could be due to underestimating water depth, overestimating bank heights, or a change in sinuosity (see Text S4 for a full discussion). In addition, we find that none of the other measured channel-system geometry parameters scale with the lateral migration rate once the rate is multiplied by the effective channel-bank height ($M_L H_b$, here defined as 'bank-sediment yield') (Figures 6B–6D). Therefore, under constant boundary conditions, autogenic changes in the effective channel-bank height (and, possibly, some changes in system-scale sinuosity) appear to explain all variability of lateral migration rates.

Interestingly, within the scatter of the data (Figure 6A), lateral migration rates of the low-Q_s experiment (Run 5, green triangles in Figure 6A) appear to follow the same scaling of migration rates with channel-bank heights as do the high-Q_s experiments (all other data in Figure 6A). Thus, in this series of experiments, a seven-fold difference in sediment discharges does not appear to significantly impact the volumetric rate of sediment reworking (Equation (2)). The low-Q_s experiment has, however, a generally lower channel slope than the high sediment-discharge experiments (Figure 6C).

© 2019 The Author. Earth Surface Processes and Landforms published by John Wiley & Sons, Ltd.

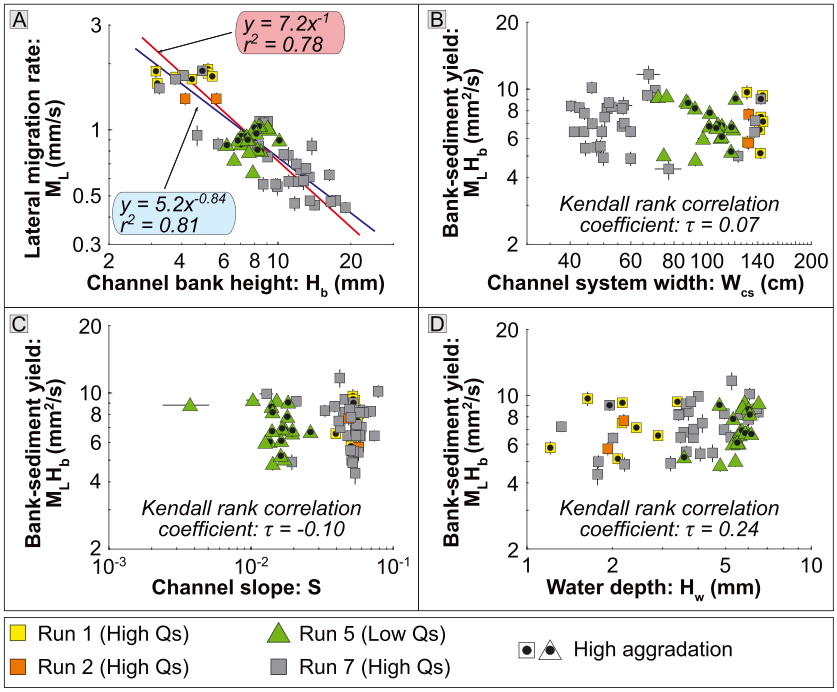

Figure 6. Controls on lateral migration rates under constant boundary conditions. (A) Lateral migration rates as a function of effective channel-bank height. Linear fits are to only the high sediment-discharge experiments using free fit parameters (blue) and with a prescribed slope of –1 (red). (B–D) Bank-sediment yield as a function of (B) channel-system width, (C) channel slope, and (D) water depth. [Colour figure can be viewed at wileyonlinelibrary.com]

We note that, during the initial aggradation period, all experiments are characterized by high channel mobility, large channel areas, large reworked areas, and low channel-constricting banks. Therefore, a scaling between aggradation rates and migration rates emerges (Figure S1C). Nevertheless, the observed relationship between migration rate and bank heights also holds when we consider only data within the range of 'steady state' aggradation and erosion rates of ~4% of the input sediment discharge (data points without a black dot in Figure 6).

Because channel geometry in our steady-state systems is self-organized, correlations between lateral migration rates and other parameters can be found. For example, the channel-system width is inversely correlated to bank heights and, therefore, strongly correlated to lateral migration rates (Figure S1B). Given these correlations, the model (Equations (2) and (3)) is the key to identifying the bank height as the mechanistically relevant parameter (Figure 6).

Controls on lateral migration rates by boundary conditions

In the previous section, we demonstrated that an inverse scaling between the effective channel-bank height and the lateral channel mobility explains most of the variability of lateral migration rates under constant boundary conditions (Figure 6). In other words, under constant boundary conditions, the bank-sediment yield ($M_L H_b$) is constant, and any autogenic variability of channel geometry that occurs independently of the bank height does not control bank sediment yield (Figures 6B–6D). As a consequence, any variability of the bank-sediment yield has to be directly linked to changes in boundary conditions, and we can find a scaling that directly links this yield to these boundary conditions without including any additional channel-system geometry parameters. Because the geometry of alluvial channels tends to adjust to the boundary conditions, an alternative expression for variations of bank-sediment yield may be expected that includes the channel-system geometry without the boundary conditions. Importantly, the two sets of variables (boundary conditions and channel-system geometry) are fundamentally dependent and cannot be mixed if their direct influence on bank-sediment yield is investigated. Here we use our results together with an existing compilation of experiments (see Table S2 and section entitled 'Compilation of experiments') in a dimensional analysis to derive and test two alternative expressions for the bank-sediment yield of braided, coarse-grained channels in non-cohesive sediment. We follow the Buckingham-π theorem (Buckingham, 1914) which states that a functional relationship between $n-k$ independent dimensionless parameters fully describes a physical process, where n is the number of variables governing the physical process and k is the number of physical dimensions (such as length and time). Once the set of n independent variables that governs the physical process is known, the $n-k$ dimensionless parameters can be chosen arbitrarily as long as (1) they are dimensionless, and (2) together, they include all n variables.

Scaling between bank-sediment yield and boundary conditions

In the first dimensional analysis, we consider as governing variables the bank sediment yield ($M_L H_b \left[\frac{L^2}{T}\right]$) and the main boundary conditions that (1) were varied in our compiled experiments and (2) have been hypothesized as major controls on lateral migration rates (Hickin & Nanson, 1984; Nanson & Hickin, 1986; Wickert et al., 2013; Constantine et al., 2014). These boundary conditions are the input water discharge ($Q_w \left[\frac{L^3}{T}\right]$), the input sediment discharge ($Q_s \left[\frac{L^3}{T}\right]$), and the grain size ($D[L]$). We explicitly do not use additional system-geometry variables because (1) they are not independent of the boundary conditions and (2) autogenic variability in channel-system geometry that occurs independently of bank heights does not

© 2019 The Author. Earth Surface Processes and Landforms published by John Wiley & Sons, Ltd.

appear to affect bank-sediment yield (Figure 6 and previous section). Given these four variables with two physical dimensions (length and time), two independent dimensionless parameters describe the physical process. Because any possible choice of the dimensionless parameters is consistent with the physically correct equations (Buckingham, 1914), the dimensional variables can be combined in the most convenient way for the problem at hand. Here, we choose a ratio of cross-stream and downstream sediment discharge (π_1) and a ratio of sediment discharge and water discharge (defined as the 'bedload concentration') (π_2)

$$\pi_1 = \frac{M_L H_b D}{Q_s}; \pi_2 = \frac{Q_s}{Q_w}. \quad (4)$$

Following the Buckingham-π theorem (Buckingham, 1914), the two parameters are related by a function *f*,

$$\pi_1 = f(\pi_2). \quad (5)$$

Here, we assume that the functional relationship can be expressed as a power law:

$$\pi_1 = k\pi_2^{\alpha} \text{ or } \frac{M_L H_b D}{Q_s} = k\left(\frac{Q_s}{Q_w}\right)^{\alpha}, \quad (6)$$

where α and k are real numbers, and k is positive, because none of the considered variables can be negative. To estimate the exponent, we combine the experimental results from this study and average values from the compilation by Wickert et al. (2013). We find that the best-fit exponent to the function in Equation (6) is $\alpha = -1.13 \pm 0.42$ ($\pm 1\sigma$) (Figure 7A). The regression fits the data reasonably well ($r^2 = 0.45$) across a five-fold range of water discharges, a nine-fold range in sediment discharges, a 15-fold range in channel-bank height, and a four-fold range in sediment grain sizes (Figure 7A and Table S2). The range of bedload concentrations ($\pi_2 = 10^{-4} - 10^{-2}$) is within the range of bedload transport rates measured for small mountain streams ($\pi_2 = 10^{-4} - 10^{-1}$) (Turowski et al., 2009; Turowski, 2010) but generally higher than ratios measured in a compilation of 93 alluvial rivers ($\pi_2 = 10^{-9} - 10^{-3}$) (Williams & Rosgen, 1989; Nittrouer et al., 2008; Nittrouer et al., 2012). The fit to the data has one notable outlier (DB03-02: Figure 7 A), a fluvial delta experiment with a 35–300-fold lower sediment discharge than the other experiments in the series (Table S2) and with subcritical flow (Martin, 2007; Wickert et al., 2013). More experiments are necessary to test the limits of the scaling and to investigate why it breaks down at very low sediment discharges and/or subcritical flow. Nevertheless, for most of the data, the analysis predicts an expression for lateral migration rates of the form:

$$M_L = k\frac{Q_w^{1.13\pm0.42} Q_s^{-0.13\pm0.42}}{H_b D}. \quad (7)$$

We hypothesize that the considerable scatter in the relationship arises because the experimental series analyzed by Wickert et al. (2013) also includes variable rates of both base-level rise ($\dot{Z}_{BL}$) and rates of basin subsidence ($\dot{Z}_{SR}$) (Table S2). Base-level rise ($\dot{Z}_{BL} > 0$) and basin subsidence ($\dot{Z}_{SR} > 0$) create accommodation space and are expected to reduce the average sediment discharge through the basin, because sediment is lost to aggradation. Conversely, base-level fall ($\dot{Z}_{BL} < 0$) and basin uplift ($\dot{Z}_{SR} < 0$) may add sediment by erosion. We, therefore, hypothesize that migration rates are modulated by both $\dot{Z}_{BL}$ and $\dot{Z}_{SR}$. The functions that describe these modifications may be complex and depend on basin geometry. Additional work is required to find physically and dimensionally sensible ways to

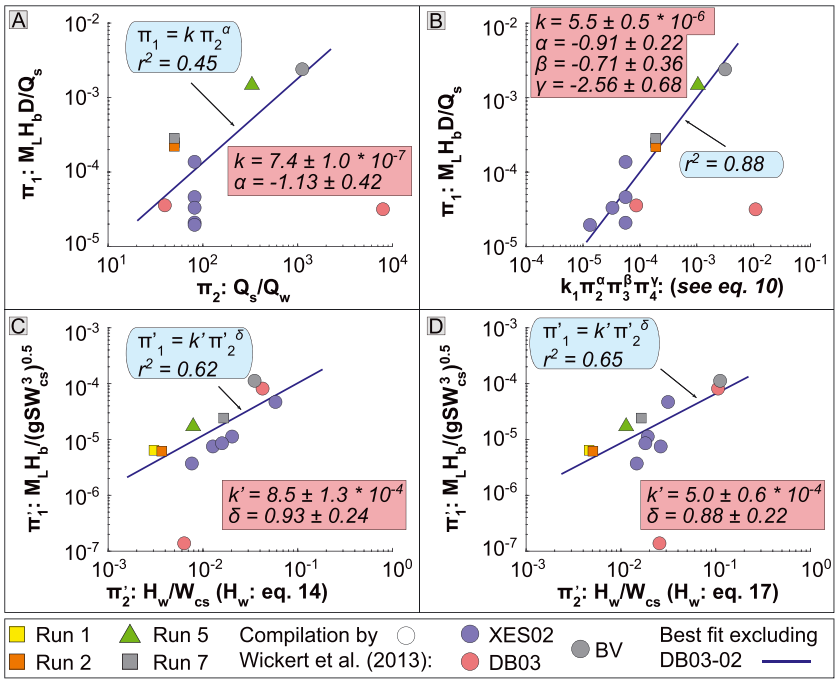

Figure 7. Regressions to non-dimensional parameters. In all plots, the regression lines ignore experiment DB03-02 (outlier in all plots). Blue text boxes: Equation and goodness-of-fit of the regression line. Red text boxes: best fit parameters with one standard error. (A) Results from the dimensional analysis explicitly considering boundary conditions, but excluding base-level changes and basin-subsidence rates. (B) Same as A but including base-level changes and basin-subsidence rates. Because the multi-variable regression cannot be shown in two dimensions, we plot the dependent non-dimensional parameter, π_1, against the product of all independent non-dimensional parameters scaled with their best-fit exponents ($\pi_2^{\alpha}\pi_3^{\beta}\pi_4^{\gamma}$) of Equation (10). (C) Results from the dimensional analysis considering channel-system geometry. Water depth was estimated using the channel-bank height (Equation (14)). (D) Same as C, but water depth was estimated using Equation (17). [Colour figure can be viewed at wileyonlinelibrary.com]

© 2019 The Author. Earth Surface Processes and Landforms published by John Wiley & Sons, Ltd.

include these variables in the analysis. Here we use a simplified approach to explore the potential utility of including these variables. For both base-level rise and basin subsidence ($\dot{Z}_{BL}$ and $\dot{Z}_{SR}$), we define two dimensionless accommodation-space factors F_{BL} and F_{SR} as:

$$\pi_3 = F_{BL} = \begin{cases} 1 + \dfrac{A_{tot}\dot{Z}_{BL}}{Q_s} \text{ for } \dot{Z}_{BL} \geq 0 \\ \dfrac{1}{\left(1 + \dfrac{A_{tot}\dot{Z}_{BL}}{Q_s}\right)} \text{ for } \dot{Z}_{BL} < 0 \end{cases} \quad (8)$$

$$\pi_4 = F_{SR} = \begin{cases} 1 + \dfrac{A_{tot}\dot{Z}_{SR}}{Q_s} \text{ for } \dot{Z}_{SR} \geq 0 \\ \dfrac{1}{\left(1 + \dfrac{A_{tot}\dot{Z}_{SR}}{Q_s}\right)} \text{ for } \dot{Z}_{SR} < 0 \end{cases} \quad (9)$$

where A_{tot} is the entire basin area. Both factors are equal to one when the accommodation space is constant ($\dot{Z}_{BL} = 0$ and $\dot{Z}_{SR} = 0$). They vary linearly with the created accommodation space ($\dot{Z}_{BL} > 0$ and $\dot{Z}_{SR} > 0$) and inversely with the destroyed accommodation space ($\dot{Z}_{BL} < 0$ and $\dot{Z}_{SR} < 0$). In all cases, the volume of created accommodation space is scaled by the input sediment discharge. This approach is highly simplified and does not account, for example, for the common observation that erosion is more localized than aggradation. Nevertheless, multi-variable regression of the equation

$$\pi_1 = k\pi_2^{\alpha}\pi_3^{\beta}\pi_4^{\gamma}; \frac{M_L H_b D}{Q_s} = k\left(\frac{Q_s}{Q_w}\right)^{\alpha} F_{BL}^{\beta} F_{SR}^{\gamma} \quad (10)$$

significantly improves the fit to the data ($r^2 = 0.88$), whereas the exponent α remains within error of the previous value ($\alpha = -0.92 \pm 0.22$ ($\pm 1\sigma$)) (Figure 7B). Similar to Equation (7), this regression predicts an expression for lateral migration rates of the form:

$$M_L = k\frac{Q_w^{0.92\pm0.22} Q_s^{0.08\pm0.22}}{H_b D} F_{BL}^{-0.71\pm0.36} F_{SR}^{-2.56\pm0.68} \quad (11)$$

Note that in this fit, we used the square of the basin length (Table S2) as a proxy for the basin area in the compiled experiments.

Scaling between bank-sediment yield and channel-system geometry

In steady state, the geometry of alluvial channels is adjusted to transport the supplied sediment with the available water discharge (Leopold & Maddock, 1953; Parker, 1979; Wickert & Schildgen, 2019). Moreover, the channel geometry may be modulated by basin subsidence and base-level changes. Therefore, the controls of the boundary conditions on bank-sediment yield should be directly reflected in a scaling between the bank-sediment yield and the remaining channel-system geometry parameters. In this second dimensional analysis, we consider the bank-sediment yield ($M_L H_b$), the channel-system width (W_{cs}), the water depth (H_w), and the slope-parallel component of the acceleration of gravity (gS) as governing variables. We specifically exclude any boundary conditions, because they are not independent of the channel geometry. We build two dimensionless groups:

$$\pi_1' = \frac{M_L H_b}{\sqrt{gSW_{cs}^3}}; \pi_2' = \frac{H_w}{W_{cs}}, \quad (12)$$

and we assume that the functional relationship between the two parameters is a power law:

$$\frac{M_L H_b}{\sqrt{gSW_{cs}^3}} = k'\left(\frac{H_w}{W_{cs}}\right)^{\delta}, \quad (13)$$

where δ and k' are real numbers. Again, k' is positive, because none of the considered variables can be negative. Because different methods were used to measure water depth in the various experiments, we can either use the bank height as a proxy for water depth:

$$H_w = H_b, \quad (14)$$

or we can obtain an estimate of the water depth from the continuity equation

$$Q_w = VW_{cs}H_w, \quad (15)$$

where V is the downstream velocity of water, and the Manning equation as derived by Gioia and Bombardelli (2001):

$$V = k_n D^{-\frac{1}{6}} H_w^{\frac{2}{3}} (gS)^{\frac{1}{2}}, \quad (16)$$

where k_n is a dimensionless and positive roughness coefficient related to Manning's roughness coefficient, n, by $k_n = \frac{D^{\frac{1}{6}}}{ng^{\frac{1}{2}}}$. Equations (15) and (16) yield:

$$H_w = \frac{D^{\frac{1}{10}} Q_w^{\frac{3}{5}}}{(gS)^{\frac{3}{10}} W_{cs}^{\frac{3}{5}} k_n}. \quad (17)$$

For both estimates of water depth, a regression of Equation (13) yields similar exponents with relatively good fits ($\delta = 0.93 \pm 0.24$ ($\pm 1\sigma$), $r^2 = 0.62$ using Equation (14), and $\delta = 0.88 \pm 0.22$ ($\pm 1\sigma$), $r^2 = 0.65$ using Equation (17)) (Figures 7C and 7D). Thus, for the lateral rate of channel migration (M_L), this analysis predicts an expression of the form:

$$\begin{aligned} M_L &= \frac{k'}{H_b}(gS)^{0.5} W_{cs}^{1.5} \left(\frac{H_w}{W_{cs}}\right)^{0.88\pm0.22} \\ &= \frac{k'}{H_b}(gS)^{0.5} W_{cs}^{0.61\pm0.22} H_w^{0.88\pm0.22}, \end{aligned} \quad (18)$$

We hypothesize that the scatter in the relationship stems from autogenic variability of the water depth, channel slope, and channel-system width that is unrelated to changes in boundary conditions and does not affect bank-sediment yield. Apart from this caveat, the effects of all major boundary conditions, including base-level rise and basin subsidence, should be reflected in the channel-system geometry: a key advantage of this approach. Thus, a direct link between lateral migration rates and channel-system geometry may, in the future, allow predictions of lateral channel-migration rates from geospatial data alone.

© 2019 The Author. Earth Surface Processes and Landforms published by John Wiley & Sons, Ltd.

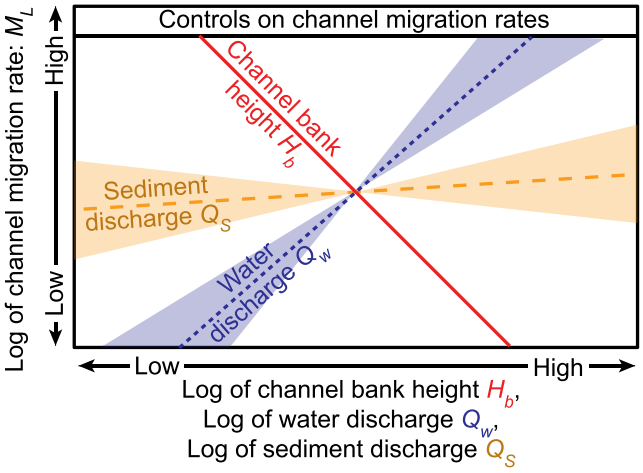

Figure 8. Conceptual sketch of the predicted variation of channel lateral migration rates with effective channel-bank height, sediment discharges, and water discharges under constant boundary conditions. Each curve assumes that all other variables remain constant. The range of slopes for water and sediment discharges are taken from Equation (11). The center point of the plot is arbitrary. [Colour figure can be viewed at wileyonlinelibrary.com]

Sensitivity of lateral migration rates

Direct influence of boundary conditions

Our analysis appears to predict that channel-bank height and water discharge exert a stronger direct control on lateral migration rates than the sediment discharge (Figure 8). The regression of dimensionless parameters $\pi_1$and π_2 remains imperfect, because our method of incorporating base-level rise and subsidence rates is limited. Nevertheless, our first-order considerations (Figures 7A and 7B) yield a strong dependence of lateral migration rates on water discharge ($M_L \sim Q_w^{1.13\pm0.42}$ according to Equation (7) and $M_L \sim Q_w^{0.92\pm0.22}$ according to Equation (11)), and only a weak dependence on sediment discharge ($M_L \sim Q_s^{-0.13\pm0.42}$ and $M_L \sim Q_s^{0.08\pm0.22}$) (Figures 7A and 7B). In contrast with these braided-channel system in non-cohesive sediment, the input sediment discharge may have a greater control on lateral migration where channel banks are cohesive, for example, due to the presence of clays or plants, and where sediment impacts are needed to erode the banks, such as in bedrock channels (Sklar & Dietrich, 2001; Fuller et al., 2016; Beer et al., 2017; Mishra et al., 2018). Our experiments have much lower Reynolds numbers and relatively large grain sizes (~1–12% of the average channel-bank height [Table S2]) compared to natural streams. Such scaling differences are common in laboratory experiments, and they may lead to differences in the behavior between experimental and natural systems. We note that many behaviors of natural channels have been recreated in the laboratory, despite differences in scaling (Paola et al., 2009), and we anticipate that our dimensional framework is applicable to natural channels. In contrast to our experiments, natural channels may be subject to varying boundary conditions, but the results should still apply where boundary conditions are not constant, because the bank sediment yield is independent of variations in channel geometry (Figure 6). Moreover, many natural streams have subcritical flow, whereas our scaling was derived for systems with supercritical flow. Therefore, to validate the framework for natural channels, it needs to be tested against field data in settings where the channel-bank height and either the input boundary conditions or the channel-system geometry are known. Interestingly, the predicted weak scaling of lateral migration rates with sediment discharge from our laboratory experiments is within one standard error of the scaling found for meandering streams of the Amazon, where $M_L \sim Q_{ss}^{0.28}$ and Q_{ss} is the suspended sediment discharge (Constantine et al., 2014). Given the difference in the channel morphology (braided channels in the experiments versus meandering channels in the Amazon), and the measured sediment discharge (total sediment discharge measured in the experiments versus suspended sediment discharge measured in the Amazon), this similarity could be a coincidence. However, perhaps it points to the potential applicability of our expression to braided and meandering natural channels.

Indirect influence of boundary conditions: controls on bank height

The earlier mentioned analysis considered the influence of boundary conditions on bank-sediment yield in steady-state systems. Therefore, for a given bank height, the scaling in Equation (11) yields the direct influence of these boundary conditions on lateral migration rates. In turn, if boundary conditions also affect bank heights, they impact lateral migration rates indirectly. Bank heights are closely linked to the evolution of channel long-profiles (Wickert & Schildgen, 2019), and perturbations in boundary conditions can have strong, non-linear, and possibly transient effects on the channel profile and on the depth of incision (Tofelde et al., 2019). For example, consider an alluvial fan that is graded (with slope, S) to transport the supplied sediment and water and has multiple active channels that rework the surface. According to hydraulic geometry relationships (Parker, 1979), we have:

$$S \sim \left(\frac{Q_s^*}{Q_w^*}\right)^{1.062} \tag{19}$$

and

$$S \sim \left(\frac{W_c^*}{Q_w^*}\right)^{0.819}, \tag{20}$$

where Q_s^* is a dimensionless input sediment discharge, Q_w^* is a dimensionless water discharge, and W^* is a dimensionless channel width. From Equation (19), a small increase in water discharge or a small decrease in sediment discharge causes a reduction in the equilibrium slope, S, and, therefore, incision. Even more incision occurs when all water is concentrated in the incised channel and the effective width of the system decreases (Equation (20)). The resulting incision and the higher channel banks should lead to a commensurate decrease of lateral mobility that may dominate the overall change in lateral migration rates. Such non-linear responses of channel mobility to changes in external drivers is supported by recent field and laboratory observations suggesting that order-of-magnitude changes in lateral channel mobility can be caused by much smaller changes in sediment discharges (Bufe et al., 2017; Grimaud et al., 2017). In Run 7 of our experimental series, all of the (up to six-fold) variability in channel-bank heights resulted from an incision event that occurred after eight hours of run-time without any change in either the input sediment or water discharges. Therefore, even autogenic (internal) redistribution of sediment and water discharges may cause significant changes in lateral mobility of streams. These effects of perturbations in boundary conditions on channel-bank heights are complex and may depend on the topography of the fluvial surface and on the geometry of the channel network. In this study, we constrained the direct effects of channel bank heights and major external boundary conditions on lateral migration

© 2019 The Author. Earth Surface Processes and Landforms published by John Wiley & Sons, Ltd.

rates. Moreover, we built a framework that can be coupled with studies on the evolution of channel long-profiles to predict the full three-dimensional adjustment of channels to external perturbations and the indirect effects of boundary conditions on lateral channel migration.

Conclusion

Based on data from three laboratory experiments, we find that lateral migration rates of a braided channel system in non-cohesive sediment scales inversely with the height of the channel banks that are being reworked by fluvial channels. This effective channel-bank height can explain almost all of the autogenic variability of lateral channel-migration rates. Using this constraint and a compilation of additional experiments in a dimensional analysis, we develop two expressions for lateral migration rates as a function of the input boundary conditions and the channel-system geometry, respectively. Our results suggest that, in steady state, the channel geometry and water discharge can exert a stronger control on lateral migration rates than does sediment discharge (Figure 8). The expressions that we provide (Equations (11) and (18)) may allow (1) prediction of migration rates of different channel systems with known external boundary conditions or (2) inversion of known channel geometries and migration rates for the external boundary conditions that affect these rivers. In turn, predicting changes in lateral migration in response to perturbations of boundary conditions requires knowledge about the effect of these perturbations on channel-bank heights. Therefore, combining this work with improved understanding of the long-profile evolution of channels (Tofelde et al., 2019; Wickert & Schildgen, 2019) could be a promising approach to constrain the coupled vertical and lateral dynamic evolution of braided gravel-bed channels.

Acknowledgements—The authors acknowledge the help of R. Christopher, J. Mullin, B. Erickson, S. Mielke, E. Steen, P. Pham, L. Horsager, K. Flemming, A. Poovey, E. Zanella and M. Barros with the set-up of the experiments. Careful reviews from Luca Malatesta, Rebecca Hodge and two anonymous reviewers greatly improved an earlier version of the manuscript. Support from National Science Foundation grant 1050070 to D.W.B. and a UCSB Graduate Student Opportunity award to A.B. is gratefully acknowledged. The project was also supported by the National Science Foundation via the National Center for Earth-surface Dynamics (NCED) under grant EAR-1246761.

Notations

Notation	Definition, [dimension]
$\alpha,\beta,\gamma,\delta$	Dimensionless fit parameters in dimensional analysis, [−]
A_{act}	Total area reworked by channels including the wetted area, $[L^2]$
A^*_{act}	Normalized active area: $A^*_{act} = \frac{A_{act}-A_{w_0}}{A_{tot}}$ [−]
A_f	Cumulative reworked area since start of the observation $t = t_0$, $[L^2]$
A^*_f	Normalized cumulative reworked area: $A^*_f = \frac{A_f-A_{w_0}}{A_{tot}}$ [−]
A_{tot}	Total analyzed area, $[L^2]$
A_w	Average wetted area over a four-hour time interval, $[L^2]$
A_{w_0}	Average wetted area at the start of observation, $[L^2]$
D	Sediment grain size, $[L]$
d_s	Search distance for effective channel-bank height measurements, $[L]$
g	Acceleration of gravity, $\left[\frac{L}{T^2}\right]$
H_b	Effective channel-bank height, $[L]$
H_w	Water depth, $[L]$
$\dot{H}$	Average aggradation rate across the investigated area, $\left[\frac{L^3}{T}\right]$
k,k'	Fit parameters, [−]
k_n	Dimensionless roughness coefficient, [−]
L_b	Length of the analyzed box, $[L]$
L_c	Characteristic length scale of the channel system, $[L]$
M_V	Volumetric rate of lateral reworking, $\left[\frac{L^3}{T}\right]$
M_L	Linear rate of lateral reworking or lateral channel-migration rate, $\left[\frac{L}{T}\right]$
n	Manning's roughness coefficient, $\left[\frac{T}{L^{\frac{1}{3}}}\right]$
p_1,p_2	Fit parameters for exponential fit, [−]
$\pi_1,\pi_2,\pi_1{}',\pi_2'$	Dimensionless parameters, [−]
Q_s	Total sediment discharge, $\left[\frac{L^3}{T}\right]$
Q_w	Water discharge, $\left[\frac{L^3}{T}\right]$
S	Channel slope, [−]
T^*_{A-M}	Channel mobility number, [−]
T_A	Characteristic timescale of avulsion, $[T]$
T_M	Characteristic timescale of lateral migration, $[T]$
t	Experimental run time, $[T]$
V	Water velocity, $\left[\frac{L}{T}\right]$
W_b	Width of the analyzed box, $[L]$
W_c	Channel width, $[L]$
W_{cs}	Channel-system width, $[L]$
$\dot{Z}_{BL}$	Base level rise rate (positive for base level rise, negative for base level fall), $\left[\frac{L}{T}\right]$
$\dot{Z}_{SR}$	Basin subsidence rate (positive for subsidence, negative for uplift), $\left[\frac{L}{T}\right]$

References

Beer AR, Turowski JM, Kirchner JW. 2017. Spatial patterns of erosion in a bedrock gorge. *Journal of Geophysical Research - Earth Surface* **122**(1): 191–214.

Bradley DN, Tucker GE. 2013. The storage time, age, and erosion hazard of laterally accreted sediment on the floodplain of a simulated meandering river. *Journal of Geophysical Research - Earth Surface* **118**(3): 1308–1319.

Buckingham E. 1914. On physically similar systems; illustrations of the use of dimensional equations. *Physical Review* **4**(4): 345–376.

Bufe A, Burbank DW, Liu L, Bookhagen B, Qin J, Chen J, Li T, Thompson Jobe JA, Yang H. 2017. Variations of lateral bedrock erosion rates control planation of uplifting folds in the foreland of the Tian Shan, NW China. *Journal of Geophysical Research - Earth Surface* **122**(12): 2431–2467.

Bufe A, Paola C, Burbank DW. 2016. Fluvial bevelling of topography controlled by lateral channel mobility and uplift rate. *Nature Geoscience* **9**(9): 706–710.

Constantine JA, Dunne T, Ahmed J, Legleiter C, Lazarus ED. 2014. Sediment supply as a driver of river meandering and floodplain evolution in the Amazon Basin. *Nature Geoscience* **7**(12): 899–903.

Coulthard TJ, Wiel MJVD. 2006. A cellular model of river meandering. *Earth Surface Processes and Landforms* **31**(1): 123–132.

© 2019 The Author. Earth Surface Processes and Landforms published by John Wiley & Sons, Ltd.

Darby SE, Rinaldi M, Dapporto S. 2007. Coupled simulations of fluvial erosion and mass wasting for cohesive river banks. *Journal of Geophysical Research - Earth Surface* **112**(F3): F03022.

Darby SE, Trieu HQ, Carling PA, Sarkkula J, Koponen J, Kummu M, Conlan I, Leyland J. 2010. A physically based model to predict hydraulic erosion of fine-grained riverbanks: the role of form roughness in limiting erosion. *Journal of Geophysical Research - Earth Surface* **115**(F4): F04003.

Dunne T, Constantine JA, Singer MB. 2010. The role of sediment transport and sediment supply in the evolution of river channel and floodplain complexity. *Transactions. Japan Geomorphological Union* **31**(2): 155–170.

Einstein A. 1926. The cause of the formation of meanders in the courses of rivers and of the so-called Baer's law. *Die Naturwissenschaften* **14**(11): 223–224.

Fuller TK, Gran KB, Sklar LS, Paola C. 2016. Lateral erosion in an experimental bedrock channel: the influence of bed roughness on erosion by bed-load impacts. *Journal of Geophysical Research - Earth Surface* **121**: 1084–1105.

Gilbert GK. 1877. *Report on the Geology of the Henry Mountains (Utah)*. Government Printing Office: Washington, DC.

Gioia G, Bombardelli FA. 2001. Scaling and similarity in rough channel flows. *Physical Review Letters* **88**(1): 014501.

Grimaud J-L, Paola C, Ellis C. 2017. Competition between uplift and transverse sedimentation in an experimental delta. *Journal of Geophysical Research - Earth Surface* **122**(7): 1339–1354.

Hancock GS, Anderson RS. 2002. Numerical modeling of fluvial strath-terrace formation in response to oscillating climate. *Geological Society of America Bulletin* **114**(9): 1131–1142.

Hanson GJ, Simon A. 2001. Erodibility of cohesive streambeds in the loess area of the midwestern USA. *Hydrological Processes* **15**(1): 23–38.

Hickin EJ, Nanson GC. 1984. Lateral migration rates of river bends. *Journal of Hydraulic Engineering* **110**(11): 1557–1567.

Howard AD, Knutson TR. 1984. Sufficient conditions for river meandering: a simulation approach. *Water Resources Research* **20**(11): 1659–1667.

Hutton D, Haque CE. 2004. Human vulnerability, dislocation and resettlement: adaptation processes of river-bank erosion-induced displacees in Bangladesh. *Disasters* **28**(1): 41–62.

Jerolmack DJ, Mohrig D. 2007. Conditions for branching in depositional rivers. *Geology* **35**(5): 463–466.

Kim W, Paola C, Swenson JB, Voller VR. 2006. Shoreline response to autogenic processes of sediment storage and release in the fluvial system. *Journal of Geophysical Research - Earth Surface* **111**: F04013. https://doi.org/10.1029/2006JF000470

Kim W, Paola C, Voller VR, Swenson JB. 2006. Experimental measurement of the relative importance of controls on shoreline migration. *Journal of Sedimentary Research* **76**(2): 270–283.

Kim W, Petter A, Straub K, Mohrig D. 2014. Investigating the autogenic process response to allogenic forcing. In *From Depositional Systems to Sedimentary Successions on the Norwegian Continental Margin, Martinius AW*, Ravnas R, Howell JA, Steel RJ, Wonham JP (eds). John Wiley & Sons: Hoboken, NJ; 127–138.

Lane EW. 1955. Importance of fluvial morphology in hydraulic engineering. In *Proceedings, volume 81, paper no. 745*. American Society of Civil Engineers: Reston, VA.

Langston AL, Tucker GE. 2018. Developing and exploring a theory for the lateral erosion of bedrock channels for use in landscape evolution models. *Earth Surface Dynamics* **6**(1): 1–27.

Leopold LB, Maddock T. 1953. *The Hydraulic Geometry of Stream Channels and Some Physiographic Implications*, Professional Paper 252. US Government Printing Office: Washington, DC.

Limaye ABS, Lamb MP. 2014. Numerical simulations of bedrock valley evolution by meandering rivers with variable bank material. *Journal of Geophysical Research - Earth Surface* **119**(4): 927–950.

Limaye ABS, Lamb MP. 2016. Numerical model predictions of autogenic fluvial terraces and comparison to climate change expectations. *Journal of Geophysical Research - Earth Surface* **121**: 512–544.

Mackin HJ. 1948. Concept of the graded river. *Geological Society of America Bulletin* **59**(5): 463–512.

Malatesta LC, Prancevic JP, Avouac J-P. 2017. Autogenic entrenchment patterns and terraces due to coupling with lateral erosion in incising alluvial channels. *Journal of Geophysical Research - Earth Surface* **122**(1): 335–355.

Martin J, Sheets B, Paola C, Hoyal D. 2009. Influence of steady base-level rise on channel mobility, shoreline migration, and scaling properties of a cohesive experimental delta. *Journal of Geophysical Research - Earth Surface* **114**(F3): F03017.

Martin JM. 2007. *Quantitative Sequence Stratigraphy*, Doctor of Philosophy. University of Minnesota: Minneapolis, MN.

Mishra J, Inoue T, Shimizu Y, Sumner T, Nelson JM. 2018. Consequences of abrading bed load on vertical and lateral bedrock erosion in a curved experimental channel. *Journal of Geophysical Research - Earth Surface* **123**(12): 3147–3161.

Muto T, Steel RJ, Swenson JB. 2007. Autostratigraphy: a framework norm for genetic stratigraphy. *Journal of Sedimentary Research* **77**(1): 2–12.

Nakamura F, Kikuchi SI. 1996. Some methodological developments in the analysis of sediment transport processes using age distribution of floodplain deposits. *Geomorphology* **16**(2): 139–145.

Nanson GC, Hickin EJ. 1983. Channel migration and incision on the Beatton River. *Journal of Hydraulic Engineering* **109**(3): 327–337.

Nanson GC, Hickin EJ. 1986. A statistical analysis of bank erosion and channel migration in western Canada. *Geological Society of America Bulletin* **97**(4): 497–504.

Nittrouer JA, Allison MA, Campanella R. 2008. Bedform transport rates for the lowermost Mississippi River. *Journal of Geophysical Research - Earth Surface* **113**(F3).

Nittrouer JA, Shaw J, Lamb MP, Mohrig D. 2012. Spatial and temporal trends for water-flow velocity and bed-material sediment transport in the lower Mississippi River. *GSA Bulletin* **124**(3–4): 400–414.

Paola C, Mullin J, Ellis C, Mohrig DC, Swenson JB, Parker G, Hickson T, Heller PL, Pratson L, Syvitski J. 2001. Experimental stratigraphy. *GSA Today* **11**(7): 4–9.

Paola C, Straub K, Mohrig D, Reinhardt L. 2009. The "unreasonable effectiveness" of stratigraphic and geomorphic experiments. *Earth-Science Reviews* **97**(1–4): 1–43.

Parker G. 1979. Hydraulic geometry of active gravel rivers. *Journal of the Hydraulics Division* **105**(9): 1185–1201.

Parker G, Shimizu Y, Wilkerson GV, Eke EC, Abad JD, Lauer JW, Paola C, Dietrich WE, Voller VR. 2011. A new framework for modeling the migration of meandering rivers. *Earth Surface Processes and Landforms* **36**(1): 70–86.

Scott ML, Auble GT, Friedman JM. 1997. Flood dependency of cottonwood establishment along the Missouri River, Montana, USA. *Ecological Applications* **7**(2): 677–690.

Sheets BA, Paola C, Kelberer JM. 2007. Creation and preservation of channel-form sand bodies in an experimental alluvial system. In *Sedimentary Processes, Environments and Basins*, Jarvis I, Nichols G, Williams E, Paola C (eds). Wiley-Blackwell: Oxford; 555–567.

Shields FD, Jr, Simon A, Steffen LJ. 2002. Reservoir effects on downstream river channel migration. *Environmental Conservation* **27**(1): 54–66.

Sklar LS, Dietrich WE. 2001. Sediment and rock strength controls on river incision into bedrock. *Geology* **29**(12): 1087–1090.

Slingerland R, Smith ND. 2004. River avulsions and their deposits. *Annual Review of Earth and Planetary Sciences* **32**(1): 257–285.

Straub KM, Paola C, Kim W, Sheets B. 2013. Experimental investigation of sediment-dominated vs. tectonics-dominated sediment transport systems in subsiding basins. *Journal of Sedimentary Research* **83**(12): 1162–1180.

Tal M, Paola C. 2007. Dynamic single-thread channels maintained by the interaction of flow and vegetation. *Geology* **35**(4): 347–350.

Tal M, Paola C. 2010. Effects of vegetation on channel morphodynamics: results and insights from laboratory experiments. *Earth Surface Processes and Landforms* **35**(9): 1014–1028.

Tofelde S, Savi S, Wickert AD, Bufe A, Schildgen TF. 2019. Alluvial channel response to environmental perturbations: fill-terrace formation and sediment-signal disruption. *Earth Surface Dynamics* **7**(2), 609–631. https://doi.org/10.5194/esurf-7-609-2019

© 2019 The Author. Earth Surface Processes and Landforms published by John Wiley & Sons, Ltd.

Torres MA, Limaye AB, Ganti V, Lamb MP, West AJ, Fischer WW. 2017. Model predictions of long-lived storage of organic carbon in river deposits. *Earth Surface Dynamics* **5**(4): 711–730.
Turowski JM. 2010. Probability distributions of bed load transport rates: a new derivation and comparison with field data. *Water Resources Research* **46**(8).
Turowski JM, Yager EM, Badoux A, Rickenmann D, Molnar P. 2009. The impact of exceptional events on erosion, bedload transport and channel stability in a step-pool channel. *Earth Surface Processes and Landforms* **34**(12): 1661–1673.
Wickert AD, Martin JM, Tal M, Kim W, Sheets B, Paola C. 2013. River channel lateral mobility: metrics, time scales, and controls. *Journal of Geophysical Research - Earth Surface* **118**(2): 396–412.
Wickert AD, Schildgen TF. 2019. Long-profile evolution of transport-limited gravel-bed rivers. *Earth Surface Dynamics* **7**(1): 17–43.
Williams GP, Rosgen DL. 1989. *Measured Total Sediment Loads (Suspended Loads and Bedloads) for 93 United States streams*, US Geological Survey, Open File Report. US Geological Survey: Reston, VA.

Supporting Information

Additional supporting information may be found online in the Supporting Information section at the end of the article.

Table S1: All parameters derived for all 4-h intervals from Runs 1,2,5,7; submitted as excel file
Table S2: All parameters from compilations of experiments submitted as excel file
Text S1: Data collection and processing
Text S2: Measurement of the active area from imagery data
Text S3: Measurement of channel geometry parameters
Text S4: Sources of uncertainty in the bank-height – migration rate scaling
Figure S1: Additional illustrations of the controls on lateral migration rates under constant boundary conditions. Lateral migration rates as a function of (A) water depth, (B) channel system width, and (C) aggradation rates. All fits are to the high sediment discharge experiments only.
Figure S2: All accepted channel mobility fits for Run 1. Af* is the normalized cumulative reworked area. A_f^*=(A_f (t)-A_(w_0))/A_tot. Blue dots are the data points, the red line is the exponential fit. The black horizontal line marks one minus the average normalized wet area at the start of the experiment. The grey lines and the grey shaded area show 2 standard deviations of the initially wet area. The title shows the 4 h time interval over which the channel mobility analysis was performed.
Figure S3: All accepted channel mobility fits for Run 2. The symbology is the same as in Figure S2.
Figure S4: All accepted channel mobility fits for Run 5 – Part 1. The symbology is the same as in Figure S2.
Figure S5: All accepted channel mobility fits for Run 5 – Part 2. The symbology is the same as in Figure S2.
Figure S6: All accepted channel mobility fits for Run 7 – Part 1. The symbology is the same as in Figure S2.
Figure S7: All accepted channel mobility fits for Run 7 – Part 2. The symbology is the same as in Figure S2.

© 2019 The Author. Earth Surface Processes and Landforms published by John Wiley & Sons, Ltd.